Nuclear Science and Techniques (2023) 34:180
https://doi.org/10.1007/s41365-023-01337-6

Measurement of Br(n,γ) cross sections up to stellar s-process temperatures at the CSNS Back-n

Gao-Le Yang[1] · Zhen-Dong An[1,2,3,4] · Wei Jiang[5,6] · Xian-Kai Li[1,7] · Wei-Wei Qiu[3,4,8] · Zheng-Fa Liao[3,4,8] · Zi-Yue Zhuang[3,4,8] · Xiao-Ping Zhang[3,4] · Sheng-Li Chen[8] · Chen-Chen Guo[8] · Er-Xi Xiao[8] · Xiao Fang[8] · Xin-Xiang Li[2,7,9] · Xin-Rong Hu[2,9] · Bing Jiang[2,9] · Jin-Cheng Wang[10] · Jie Ren[10] · Wen Luo[7] · Zhi-Chao Zhu[7] · Hao-Yang Lan[7] · Zong-Wei Cao[7] · Xu Ma[10,11] · Ying-Du Liu[11] · Pu-Sen Wang[11] · Yi Yang[12] · Ping Su[12] · Xian-Gai Deng[12] · Wan-Bing He[12] · Chun-Wang Ma[13,14] · Yu-Ting Wang[13,14] · Zhi-Tao Dai[15] · Peng-Qin He[1] · Ren-Guang Tang[1] · Tao Zhou[1] · Jing Wang[1] · Han Yi[5,6] · Yue Zhang[5,6] · Yong-Hao Chen[5,6] · Rui-Rui Fan[5,6] · Ke-Qing Gao[5,6] · Qiang Li[5,6] · Kang Sun[5,6] · Zhi-Xin Tan[5,6] · Min-Hao Gu[5,6] · Han-Tao Jing[5,6] · Jing-Yu Tang[5,6,16] · The CSNS Back-n Collaboration

Received: 8 May 2023 / Revised: 4 October 2023 / Accepted: 9 October 2023 / Published online: 29 November 2023

Abstract
The neutron capture cross sections (n, γ) of bromine were obtained using the time-of-flight technique at the Back-n facility of the China Spallation Neutron Source. Prompt γ-rays originating from neutron-induced capture events were detected using four C_6D_6 detectors. The pulse-height weighting technique and double-bunch unfolding method based on Bayesian theory were used in the data analysis. Background deductions, normalization, and corrections were carefully considered to obtain reliable measurement results. The multilevel R-matrix Bayesian code SAMMY was used to extract the resonance parameters in the resolved resonance region (RRR). The average cross sections in the unresolved resonance region (URR) were obtained from 10 to 400 keV. The experimental results were compared with data from several evaluated libraries and previous experiments in the RRR and URR. The TALYS code was used to describe the average cross sections in the URR. The astrophysical Maxwell average cross sections (MACSs) of ^{79,81}Br from $kT = 5$ to 100 keV were calculated over a sufficiently wide range of neutron energies. At a thermal energy of $kT = 30$ keV, the MACS value for ^{79}Br 682±68 mb was in good agreement with the KADoNiS v1.0 recommended value. By contrast, the value of 293±29 mb for ^{81}Br was substantially higher than that of the evaluated database and the KADoNiS v1.0 recommended value.

Keywords Time-of-flight technique · Neutron capture cross sections · Maxwell average cross sections

1 Introduction

Elements heavier than iron are mainly produced by two neutron capture processes, the *s*(slow)- and *r*(rapid)-processes, both contributing approximately half of the observed solar abundances [1]. Since 1957, the majority of progress has been made in the field of the *s*-process. It has become apparent that a single *s*-process is insufficient to explain the observed solar abundances. At least two components, the main and weak s-processes, are necessary and can be connected to the corresponding stellar objects and sites [2, 3]. The main s-process occurs in the He-rich inner shell of thermally pulsing asymptotic giant branch (AGB) stars and predominantly produces nuclei with mass number A>90. The weak component, which is responsible for the production of

This work was supported by the National Natural Science Foundation of China (Nos. U1832182, 11875328, 11761161001, and U2032137), the Natural Science Foundation of Guangdong Province, China (Nos. 18zxxt65 and 2022A1515011184), the Science and Technology Development Fund, Macau SAR (Grant No. 008/2017/AFJ), the Macao Young Scholars Program of China (No. AM201907), the China Postdoctoral Science Foundation (Nos. 2016LH0045 and 2017M621573), and the Fundamental Research Funds for the Central Universities (Nos. 22qntd3101 and 2021qntd28).

Extended author information available on the last page of the article

nuclei between iron and yttrium (56<A<90), occurs during the convective core He burning stage in massive stars [1]. Because the neutron exposure is small, the weak s-process flow cannot overcome the bottleneck at the closed neutron shell N= 50 [4].

The s-process components of solar abundances in the Br-Kr-Rb region are characterized by the superposition of abundance contributions from the main s-process associated with thermally pulsing low-mass AGB stars and from the weak s-process [5, 6]. However, these two components have different contributions. While the relative strength of the weak component decreases significantly with increasing mass number, that of the main component increases rapidly. The complexity of this situation is further enhanced if one recalls that the weak and main s-processes exhibit two very different neutron capture regimes. The branches in this regime are shown in Fig. 1 to represent the most problematic part of the s-process path. Quantitative investigations of these aspects rely on an accurate stellar (n, γ) cross section. Furthermore, lanthanum bromide detectors are used in nuclear experiments for neutron and γ-ray detection, and accurate and reliable experimental data for neutron-induced reactions are required for detector design and optimization.

Regarding the available data for Br, previous time-of-flight (TOF) experiments and studies based on activation techniques mainly focused on the unresolved resonance region (URR) [7–9]. Figure 2 shows the previous experimental (n,γ) cross sections of bromine. Gibbons et al. [10], Ohkubo et al. [11] and Macklin [12] measured the neutron resonance parameters of ^{79}Br and ^{81}Br using an electron accelerator neutron source. Our study was conducted at the back-streaming white neutron beam line (Back-n) of the China Spallation Neutron Source (CSNS) [13–15]. Deexcited γ-rays were detected using four hydrogen-free deuterated benzene (C_6D_6) liquid scintillator detectors [16–18]. A

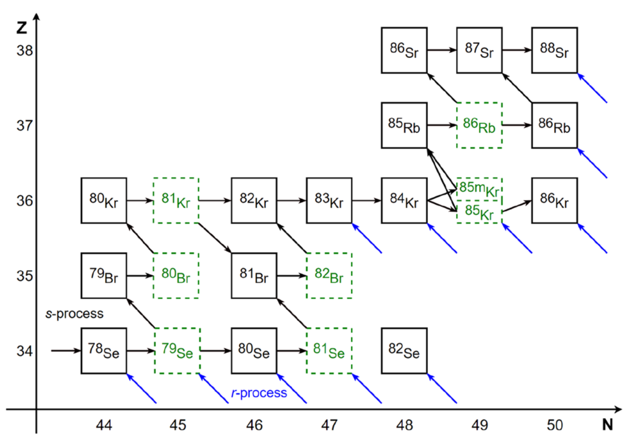

Fig. 1 Nucleosynthesis processes occurring in the region among Br. The s- and r-processes are indicated by black and blue arrows, respectively

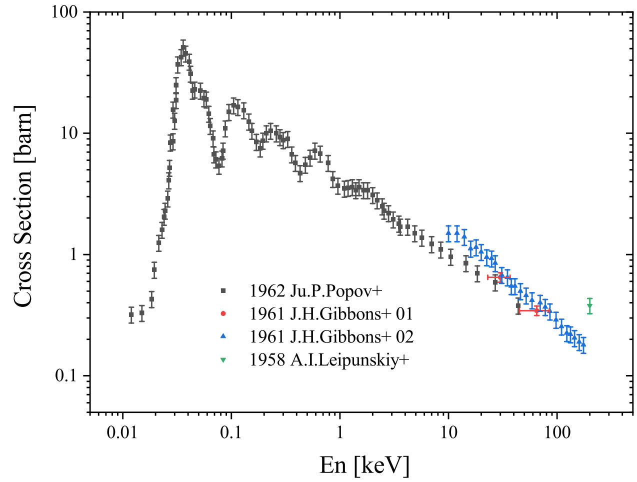

Fig. 2 Previous experimentally measured cross sections of ^{nat}Br (n,γ) compiled in the EXFOR database

^{6}LiF–Si detector array was used as a beam monitor for real-time online monitoring of neutron flux on the white neutron source [19, 20]. The experimental conditions of the Back-n facility used in this study and the corresponding experimental setup are described in Sect. 2. The data analysis is provided in Sect. 3, including the pulse-height weighting technique (PHWT), double-bunch unfolding method, background deductions, normalization, and corrections. A theoretical description of the experimental results is presented in Sect. 4. Finally, the conclusions are presented in Sect. 5.

2 Measurements

Measurements were made using the C_6D_6 detector system in the Back-n facility of the CSNS [21, 22]. Neutrons were produced by slamming a 1.6 GeV/c^2 proton beam with double bunches per pulse onto a tungsten target with a typical repetition rate of 25 Hz [23, 24]. The pulse width of each bunch was 41 ns, and the interval between the two bunches was 410 ns [25]. There were two experimental stations along the neutron beam line: a near station (ES#1), 56 m from the spallation target to the sample, and a far station (ES#2) with a 76-m neutron flight path [21]. The detector system for the (n,γ) reaction measurement consisted of four C_6D_6 detectors, aluminum detector brackets, and an aluminum sample holder, as shown in Fig. 3. The C_6D_6 detectors were placed upstream of the sample, and the detector axis was set at an angle of 110° relative to the neutron beam [20]. A ^{6}LiF–Si detector array with a 360 μg/cm^2 ^{6}LiF neutron conversion layer and eight separated Si detectors was used for neutron flux monitoring. Signals from these detectors were processed by a generalized full-waveform digital data

Fig. 3 (Color online) Photograph of the C_6D_6 detector system in the Back-n facility of the CSNS. A gold sample is placed in the aluminum sample holder

acquisition system in which flash analog-to-digital converters were based on folding-ADC and FPGA techniques. Each channel had a digital resolution of 12 bits and a sampling rate of 1 GSPS, corresponding to a time step of 1 ns/sample. The digital waveform data of the detectors were filtered using a fully digital trigger system and then transferred to the CSNS computation center for long-term storage [19].

Our study was conducted at experimental station ES#2. The shutter and collimators had an inner diameter of $\Phi 50 + \Phi 15 + \Phi 40$ mm, resulting in a circular Gaussian-shaped beam profile with a diameter of approximately 40 mm at the sample position [25]. A thin foil of a cadmium absorber was placed at the front of the neutron shutter to absorb neutrons with an energy lower than 0.5 eV to avoid the overlap between consecutive neutron pulses[26, 27]. In addition, a Ta—Ag—Co filter with a total thickness of 1.0+0.4+1.4 mm was used to determine the in-beam γ-ray background by employing the black resonance method[28, 29]. Five samples were used in the measurements: (i) a KBr crystal, (ii) a ^{197}Au sample for experimental setup verification and flux normalization, (iii) a natural carbon sample, (iv) a lead sample to determine the background due to scattered neutrons and in-beam γ rays, and (v) an empty target to determine the sample-independent background. In the experiments, the samples were fixed to the aluminum sample holder of the C_6D_6 detector system. The characteristics of the samples and the experimental duration are summarized in Table 1.

3 Data analysis

3.1 PHWT

The efficiency of the C_6D_6 detectors in detecting neutron capture events depends on the de-excitation paths of the compound nucleus, which are too complex to be calculated [30]. The PHWT is required in the measurements to manipulate the response function of the C_6D_6 detector for γ-rays. Thus, the detection efficiency (ϵ_γ) for γ-rays with energy E_γ satisfies

$$\epsilon_\gamma = c \cdot E_\gamma, \tag{1}$$

where c is the proportionality coefficient. When ϵ_γ is sufficiently low ($\epsilon_\gamma \ll 1$), the efficiency of detecting a capture event (ϵ_c) can be described as

$$\epsilon_c \simeq \sum_{i=1}^{N} \epsilon_{\gamma i} = c \sum_{i=1}^{N} E_{\gamma i} = c \cdot (S_n + E_n), \tag{2}$$

where S_n is the neutron binding energy of the compound nuclei, $E_{\gamma i}$ is the ith cascading γ-ray energy, and E_n is the kinetic energy of the incident neutron at the center of the mass system. In this study, $S_n = 7.89$ MeV and 7.59 MeV for the compound nuclei of ^{79}Br and ^{81}Br, respectively. However, only a single S_n value can be used in Eq. (2). The method in ref. [31] was adopted in this study, S_n of the most abundant isotope in the sample (^{79}Br) was chosen, and the abundance of ^{81}Br isotopes in the sample was scaled according to its S_n value. In this case, the deviation caused by the selected S_n was less than 3%. The manipulation mentioned above was implemented using a weighting function (WF) [30]. The detector count of each depositional energy was multiplied

Table 1 Characteristics of the samples and experimental duration of our experiments

Target	Mass (g)	Diameter (mm)	Thickness (mm)	Purity (%)	Experimental eq-eg duration (h)	
					Without filter	With filter
^{197}Au	4.83 ± 0.01	40.0 ± 0.02	0.20 ± 0.02	≥ 99.99	11.0	4.0
KBr	11.17 ± 0.01	30.0 ± 0.02	2.0 ± 0.02	≥ 99.99	23.5	4.5
^{nat}Pb	13.93 ± 0.01	40.0 ± 0.02	0.98 ± 0.02	≥ 99.9	8.0	–
^{nat}C	2.86 ± 0.01	40.0 ± 0.02	1.02 ± 0.02	≥ 99.9	8.7	–
empty	–	–	–	–	8.0	6.0

by the WF to correct for the original γ-ray efficiency of the detectors and hence achieve the relationship expressed in Eq. (1). In this study, energy and resolution calibrations for each individual C_6D_6 detector were performed using standard γ-ray sources, including ^{60}Co and ^{137}Cs. A realistic Monte Carlo simulation of the experimental conditions and target setup was performed using the Geant4 [32] toolkit and used to obtain an accurate response function. Finally, a least-squares method minimizing

$$\chi^2 = \sum_i \left(cE_{\gamma i} - \int_{E_\mathrm{L}}^{\infty} R(E_\mathrm{d}, E_{\gamma i}) WF(E_\mathrm{d}) \mathrm{d}E_\mathrm{d} \right)^2 \tag{3}$$

was used to determine the WF, where i is the group of mono-energetic γ-rays used in the simulation, E_L is the low-deposited energy threshold of the C_6D_6 detector, and $R(E_\mathrm{d}, E_{\gamma i})$ is the detector response function. The WF of the natural KBr and gold samples were determined independently using this method as shown in Fig. 4. A detailed study of the possible sources of systematic uncertainties revealed that the PHWT had an accuracy of 3% [33].

3.2 Double-bunch unfolding method

At present, the accelerator complex of the CSNS operates in the normal mode, where each pulse contains two proton bunches, and the interval between the two bunches is 410 ns [13]. The neutrons generated by the two proton bunches overlap with each other. Thus, the neutron energy resolution of TOF measurement is reduced, particularly in the higher-neutron-energy region (above hundreds of eV). An unfolding method based on Bayes' theorem was developed by Yi et al. [34] to obtain better time and energy resolutions.

In the normal mode of the CSNS, the two bunches in each single-beam pulse are essentially identical, and the temporal structure is extremely reproducible from pulse to pulse, as shown in Refs. [13, 34]. For the statistical time count spectrum measured in the normal mode, the counts of each time bin E_i measured in such a mode should theoretically depend on the counts C_i measured in the single-bunch mode. The transformation from the single-bunch mode spectrum to the normal mode spectrum can be written in the form of a matrix as

$$\boldsymbol{E} = \boldsymbol{R} \cdot \boldsymbol{C}, \tag{4}$$

where the vectors $\boldsymbol{E} = (E_0, \cdots, E_i, \cdots, E_n)$ and $\boldsymbol{C} = (C_0, \cdots, C_i, \cdots, C_n)$, and the transformation matrix $\boldsymbol{R}$ can be expressed as

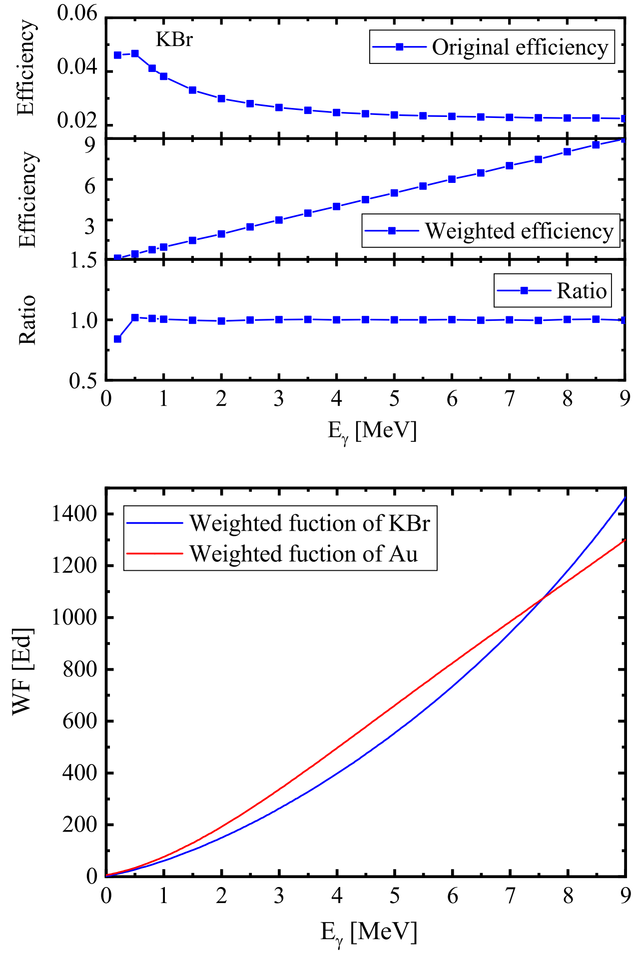

Fig. 4 (Color online) **a** Original efficiency of the C_6D_6 detector; **b** efficiency of the detector weighted by the WF; **c** coefficient of the weighted efficiency vs incident γ-ray energy; **d** WF of the C_6D_6 detector system with KBr and Au samples

$$\boldsymbol{R} = \begin{bmatrix} R_{11} & & & & & \\ \vdots & R_{22} & & & & \\ R_{(1+\Delta)1} & \vdots & \ddots & & & \\ & R_{(2+\Delta)2} & \vdots & R_{ii} & & \\ & & \ddots & \vdots & \ddots & \\ & & & R_{n(n-\Delta)} & \cdots & R_{nn} \end{bmatrix}, \tag{5}$$

where Δ is the number of bins corresponding to the offset of the double-bunch interval (410 ns), and $R_{ij} = \frac{1}{2}$ if $i = j$ or $j = i - \Delta$; otherwise, $R_{ij} = 0$. Using Eq. (5), the unfolding problem can be treated as an inverse matrix problem. However, the inverse matrix method occasionally yields several negative-value bins and oscillations caused by statistical uncertainty in the measurements. Thus, an iterative algorithm using Bayesian estimation was developed, and the inverse matrix problem can be replaced by an iterative process [34, 35]:

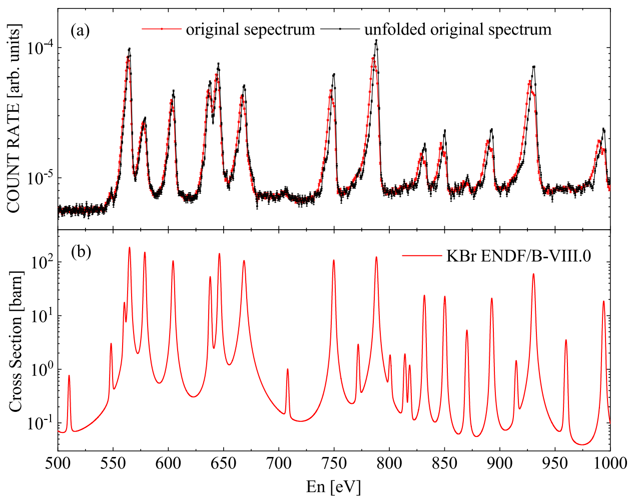

Fig. 5 (Color online) **a** Comparison between the weighted original spectrum of the KBr sample (black curve) and the weighted original spectrum obtained from the unfolding process (red curve); **b** ENDF/B-VIII.0 database of KBr. In panel (**a**), the black curve shows the presence of clear double peaks caused by the double-bunch beam structure, whereas the resonance structures are restored when using the unfolding procedure, as indicated by the red curve

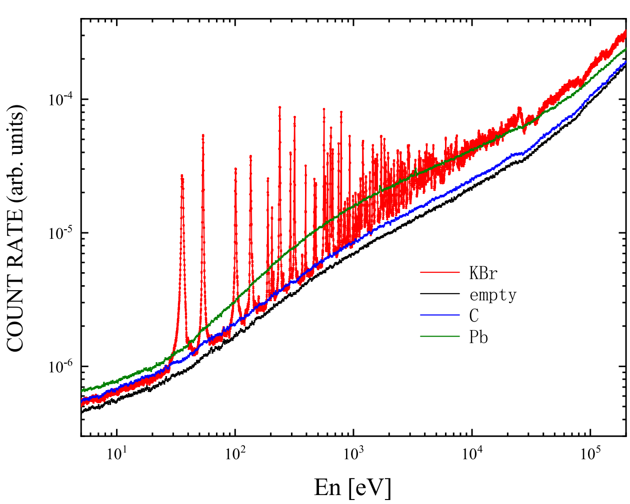

Fig. 6 (Color online) Preprocessed and normalized (according to the proton beam number) original spectra of KBr, $^{\mathrm{nat}}$C, $^{\mathrm{nat}}$Pb, and the empty target

$$\bar{C}_i^{k+1} = E_i \frac{C_i^{(k)}}{C_{i-\Delta}^{(k)} + C_i^{(k)}} + E_{i+\Delta} \frac{C_i^{(k)}}{C_i^{(k)} + C_{i+\Delta}^{(k)}}, \tag{6}$$

where $C_i^{(k)}$ indicates the result of the kth iteration and the initial $C_i^{(0)}$ is set as E_i measured in the double-bunch distribution. Some unfolding results for a KBr target are shown in Fig. 5

The original spectra preprocessed using the PHWT and double-bunch unfolding methods were normalized using the proton beam number, as shown in Fig. 6.

3.3 Background

There are two types of components contributing to the background level in captured cross-section measurements with C_6D_6 detectors [36]: sample-dependent background $B_{\mathrm{sample}}(t_{\mathrm{n}})$ and sample-independent background $B_{\mathrm{empty}}(t_{\mathrm{n}})$; that is,

$$B(t_{\mathrm{n}}) = B_{\mathrm{empty}}(t_{\mathrm{n}}) + B_{\mathrm{sample}}(t_{\mathrm{n}}). \tag{7}$$

The contribution of $B_{\mathrm{empty}}(t_{\mathrm{n}})$ can be measured directly using an empty sample under the same experimental conditions. On the other hand, the sample-dependent background $B_{\mathrm{sample}}(t_{\mathrm{n}})$ is caused by interactions between the sample and all types of in-beam particles, including the scattered-neutron-induced background $B_{\mathrm{sn}}(t_{\mathrm{n}})$, scattered in-beam γ-rays background $B_{\mathrm{s}\gamma}(t_{\mathrm{n}})$, and sample activation background $B_{\mathrm{ac.}}$. Thus, the sample-dependent background can be expressed as [36]

$$B_{\mathrm{sample}}(t_{\mathrm{n}}) = B_{\mathrm{sn}}(t_{\mathrm{n}}) + B_{\mathrm{s}\gamma}(t_{\mathrm{n}}) + B_{\mathrm{ac}}. \tag{8}$$

The scattered-neutron-induced background $B_{\mathrm{sn}}(t_{\mathrm{n}})$ can be determined using carbon sample measurement [37],

$$B_{\mathrm{sn}}(t_{\mathrm{n}}) = \frac{Y_{\mathrm{Br,\,el}}}{Y_{\mathrm{C,\,el}}} \left(W \cdot C_{\mathrm{C}}(t_{\mathrm{n}}) - W \cdot C_{\mathrm{empty}}(t_{\mathrm{n}}) \right), \tag{9}$$

where $Y_{\mathrm{C,\,el}}$ and $Y_{\mathrm{Br,\,el}}$ are the neutron scattering yields of the carbon and bromine targets obtained from the database, and $W \cdot C_{\mathrm{C}}(t_{\mathrm{n}})$ and $W \cdot C_{\mathrm{empty}}(t_{\mathrm{n}})$ are the normalized weighted counts of the carbon and empty samples, respectively. The in-beam γ-rays originated from neutron capture in the water moderator of the spallation source. Indeed, these γ-rays could be scattered by the sample. The target and energy dependence of in-beam γ-ray background components were determined from a measurement of a lead sample and the absorption valleys of 4.28 eV, 5.18 eV, 132 eV, and 5.02 keV of the Ta–Ag–Co filter, as shown in Fig. 7. As shown in this figure, the empty background $B_{\mathrm{empty}}(t_{\mathrm{n}})$ was subtracted from all the spectra, and the background due to the scattered neutrons from the lead sample was subtracted using Eq. (9). The figure also shows the activation background that was determined by fitting the spectral platform above 11 ms ($E_{\mathrm{n}} \approx 0.2$ eV) [36]. In this region, the neutrons were absorbed by the cadmium absorber, and the in-beam γ-rays could be ignored; the counts in the residual TOF spectrum were attributed to the activation of the sample and surrounding materials. In Fig. 7a, the absorption valley at 5 keV did not match the in-beam gamma-ray background shape

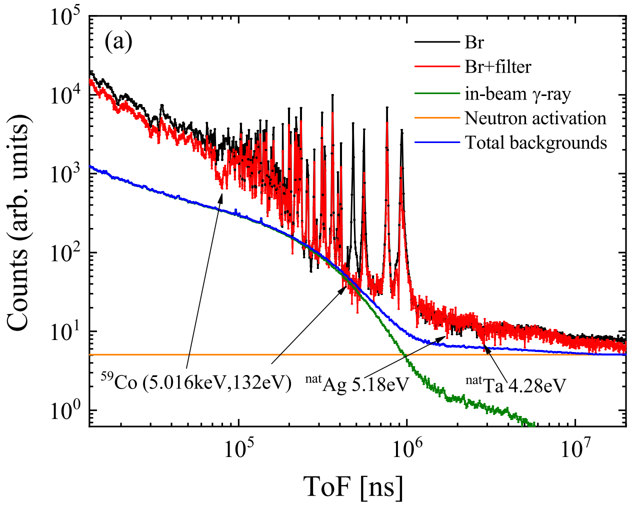

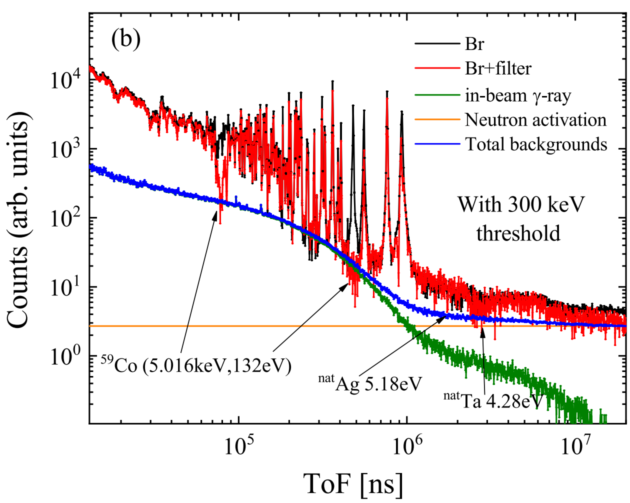

Fig. 7 (Color online) **a** Measured in-beam γ-ray backgrounds are normalized to match the values of the energies of the black resonances, namely 4.28 eV (Ta filter), 5.18 eV (Ag filter), and 132 eV, and 5.016 keV (Co filter). **b** A threshold of 300 keV is used to avoid the influence of the 536 keV level

determined by the Pb target. We believe that this was caused by delayed gamma-rays from the inelastic scattering reaction channel of ^{81}Br. ^{81}Br contained a 536.2 keV level with a lifetime of 34.6 μs, and the inelastic scattering reaction channel of ^{81}Br opened with a neutron energy greater than 500 keV (flight time of 15 μs for the Back-n facility). The flight time of the 5-keV absorption valley was approximately 80 μs. In the region of the 5 keV absorption valley, the delayed gamma-ray from ^{81}Br contributed to some additional gamma-ray counts. However, the flight time for the 132 eV absorption valley was 460 μs, which is far greater than the lifetime of the 536.2 keV level. Therefore, we used the 132 eV black resonance to determine the in-beam gamma-ray background for the KBr crystal. The 536.2 keV level will deexcite through gamma-rays of 260.2 keV and 276 keV.

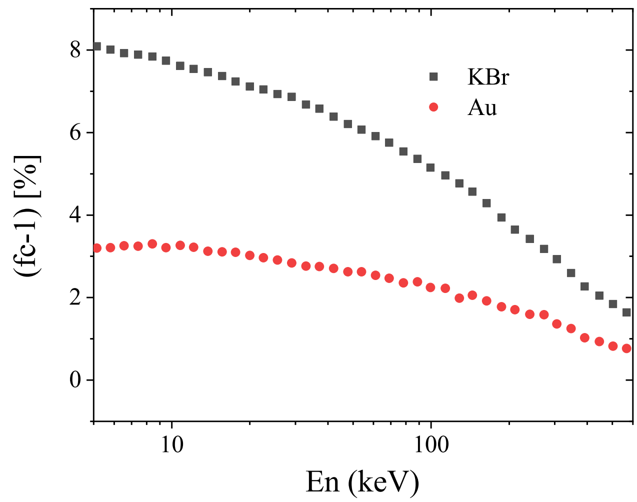

Fig. 8 Correction factor for the multiple scattering events and self-shielding calculated using the Geant4 toolkit. The black solid dots represent natural Bromine, whereas the red solid dots represent the gold sample

Thus, a threshold of 300 keV was used in the experimental data to verify this hypothesis; the results are shown in Fig. 7 (b). In this figure, the absorption valleys at both 132 eV and 5.02 keV agree with the in-beam gamma-ray background shape determined by the Pb target. However, the majority of the gamma-ray energy released by the composite nuclear decay generated by neutron capture was also below 300 keV; therefore, this threshold was not used in the experimental data processing.

3.4 Experimental corrections and absolute neutron flux normalization

For the RRR, sample-related corrections were included in the SAMMY [38] analysis. In the URR, multiple neutron scattering events and self-shielding corrections in the sample were determined through Geant4 simulations, as shown in Fig. 8.

$$\sigma_\gamma = \frac{N_\mathrm{w}}{IS_\mathrm{n}} \times \frac{\sigma_\mathrm{t}}{1 - \exp{(Nf_\mathrm{c}t\sigma_\mathrm{t})}}, \tag{10}$$

where f_c is the correction factor for multiple scattering events and self-shielding effects, and N is the area density in atoms/barn of the sample, which was 0.00339 atoms/barn for the bromine sample and 0.00117 atoms/barn for the gold sample. The uncertainty of the f_c factor was considered to be 1%. The relative normalization of the well-defined energy dependence of the neutron flux could be obtained from various runs using the Li–Si neutron detectors in ES#1. The absolute flux was determined using the gold reference sample with the (n,γ) cross section of ^{197}Au as a standard.

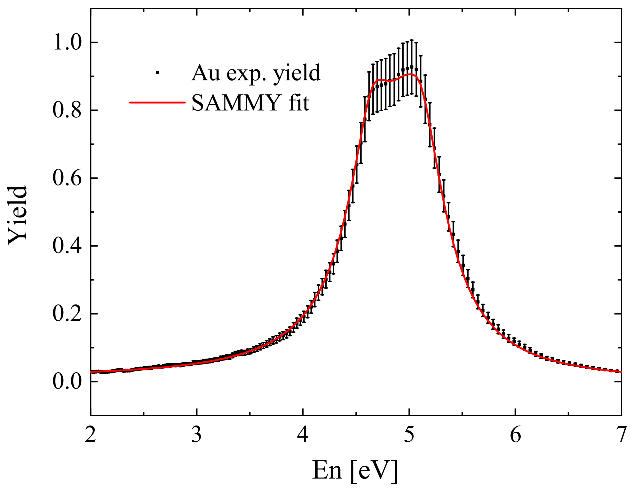

Fig. 9 Capture yield of the first resonance of ^{197}Au (4.9 eV) measured at the Back-n facility and normalized by the SAMMY [38] fit

The first gold resonance at 4.9 eV was used to define the flux in the RRR using the saturated-resonance method, as shown in Fig. 9. The absolute yield normalization was determined through a fit of the gold target data using the R-matrix code SAMMY [38, 39] and by adopting the resonance parameters of Ref. [37]. A systematic uncertainty of 1.5% was adopted for absolute flux normalization. In the keV region, the average (n,γ) cross sections were obtained relative to gold. The background of the Au spectrum was determined using the same method as that used for the bromine spectra.

3.5 Discussion of the uncertainties

The total uncertainties, including the statistical and systematic, are discussed. The statistical uncertainty originated from the raw counts in an energy bin of four samples and was estimated to be <2.0%. In fact, because raw counts change depending on the width of the energy bins and the value of the (n, γ) cross sections, wider energy bins help to increase the counts and reduce the statistical error for energy >2.0 keV. However, energy bins that are too wide cannot exhibit a fine resonance structure.

The systematic uncertainty was mainly due to the uncertainty of the experimental conditions and data analysis method. There were several types of uncertainties in the experimental conditions, including the uncertainty of the sample parameter, beam profile of the sample, neutron energy spectrum, and proton beam power. The uncertainty of the data analysis method was mainly caused by the PHWT method, double-bunch unfolding process, normalization, background subtraction, and correction in the URR. Finally, according to error propagation, the overall experimental uncertainty was less than 10.60%, as shown in Table 2. This large error was primarily due to the uncertainty of the neutron spectrum (<8%). Therefore, a good neutron energy spectrum with a lower uncertainty would significantly improve the accuracy of this experiment.

Table 2 Statistical and systematic uncertainties of the experiment

Component	Uncertainty (%)
PHWT	3.0
Unfolding method	3.0
Normalization	1.5
Background subtraction	2.0
Experimental corrections	1.0
Proton beam power	1.5
Neutron beam profile	1.5
Target parameters	0.1
Neutron spectrum ($\geq$ 0.15 MeV)	4.5
Neutron spectrum ($\leq$ 0.15 MeV)	8.0
Statistical	2.0
Total uncertainty($\geq$ 0.15 MeV)	8.2
Total uncertainty($\leq$ 0.15 MeV)	10.6

4 Results and discussion

4.1 R-matrix fits

In the region of 1 to 2000 eV, the capture yields were analyzed using the R-matrix analysis code SAMMY [38]. The yield was parameterized via the Reich-Moore approximation to the R-matrix formalism. A scattering radius of 6.85 fm and a temperature of 293 K were adopted for the correction of the Doppler effect. Other experimental effects, that is, multiple neutron scattering in the sample and neutron self-shielding, are properly taken into account within the SAMMY code. Resonance broadening owing to the neutron energy resolution function was also considered in the SAMMY fit through the implemented RPI parameterization [40].

The fitting procedure allowed us to extract the resonance parameters (radiation width Γ_γ, neutron width Γ_n, and orbital angular momentum L, etc.) from the measured capture yields. However, in many cases, only the resonance energy E_R and total capture kernel k should be considered as real measurable quantities. The capture kernel k is proportional to the area under an isolated resonance and is given by

$$k = g\Gamma_n\Gamma_\gamma/\Gamma, \tag{11}$$

where g is a statistical factor defined as

$$g = \frac{2\boldsymbol{J}+1}{(2\boldsymbol{s}+1)(2\boldsymbol{I}+1)}, \tag{12}$$

where $\boldsymbol{J}$ is the total angular momentum, $\boldsymbol{s}$ is the spin of the incident particles ($\boldsymbol{s} = \frac{1}{2}$ for neutrons), and $\boldsymbol{I}$ is the spin of the target particles.

The resonance parameters of bromine in the Evaluated Nuclear Data Files (ENDF/B-VIII.0) database were adopted as the initial parameters for the SAMMY fitting procedure. The resonance parameters from the ENDF/B-VIII.0 database are consistent with the measurements of Macklin [12], but it contains resonances that are smaller than those of Ohkubo et al. [11]. The final SAMMY-fitted results for the KBr crystal capture yield are shown in Fig. 10. The black data represent the experimental capture yield measured in this study, and the red solid curve is the actual SAMMY fit to the present data. The fitted resonance parameters and radiative kernels derived using Eq. (11) are listed in Table 5.

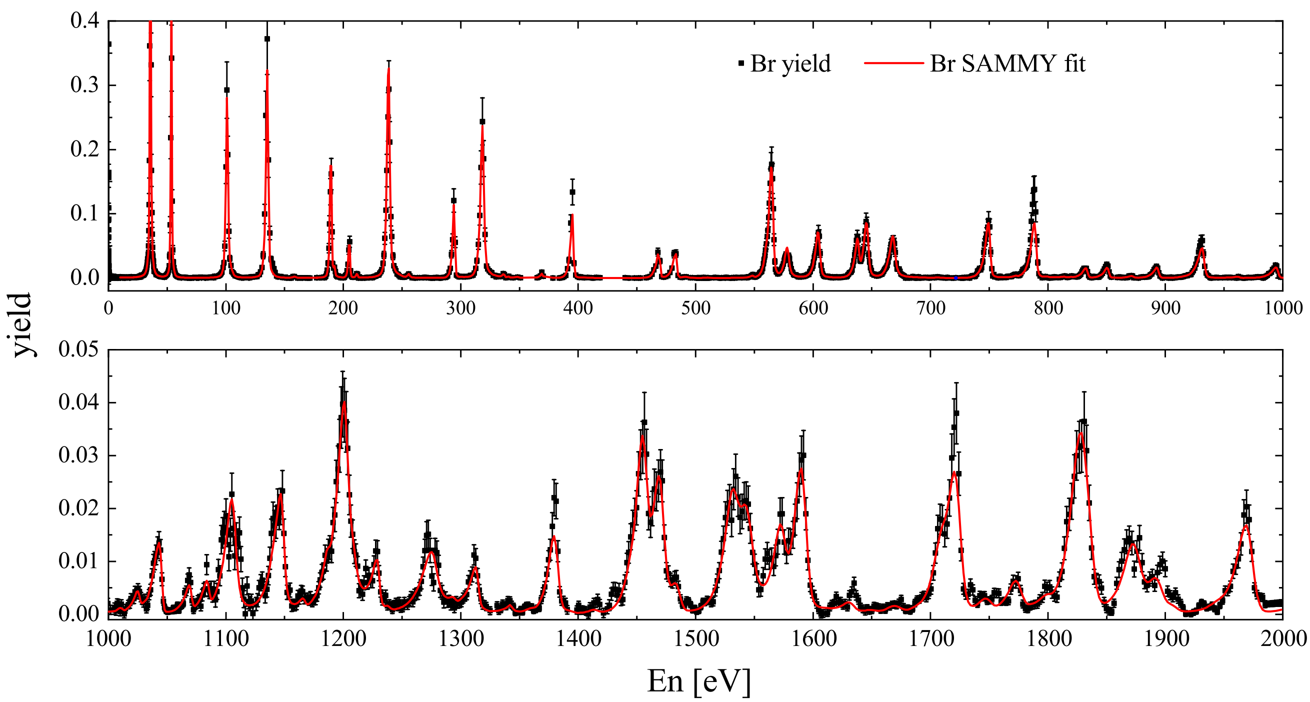

Fig. 10 (Color online) Analysis of the resonance parameters of the experimental data fitted by the R-matrix code SAMMY

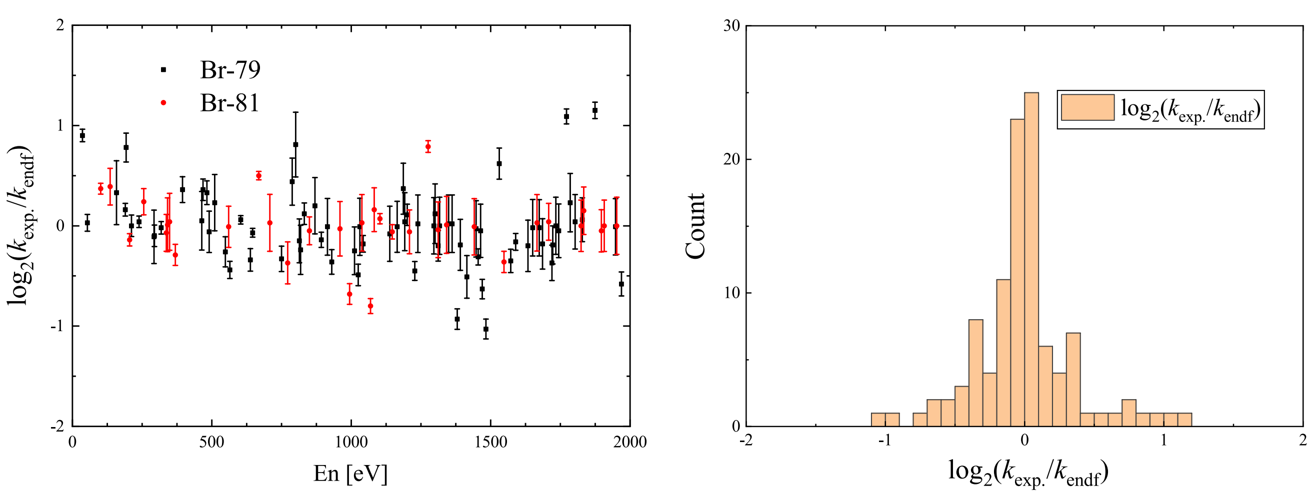

Fig. 11 (Color online) **a** Ratio of the capture kernels obtained from the ENDF/B-VIII.0 database and the present C_6D_6 results as a function of the resonance energy. **b** Corresponding distribution of the ratios

The contributions of ^{39,41}K were considered using the resonance parameters from the ENDF/B-VIII.0 database. And the ratio of the capture kernels obtained from the ENDF/B-VIII.0 database and the fitted resonance parameters is shown in Fig. 11.

For comparison with the evaluated databases, we calculated the neutron capture cross section $\sigma_{\text{exp.}}(\text{n},\gamma)$ for Br with our experimental yield $Y_{\text{exp.}}(\text{n},\gamma)$,

$$\sigma_{\text{exp.}}(\text{n},\gamma) = \frac{Y_{\text{exp.}}(\text{n},\gamma)\sigma_{\text{tot}}}{(1-e^{-N\sigma_{\text{tot}}})} \tag{13}$$

where σ_{tot} is the total cross section calculated from the ENDF/B-VIII.0 database and N is the atomic number density of Br in the KBr crystal. The calculated $\sigma_{\text{exp.}}(\text{n},\gamma)$ are plotted as blue dots in Fig. 12.

4.2 Statistical analysis

The present set of resonance parameters was used for statistical analysis to determine the nuclear properties required for the cross-section calculations [39]. The cumulative number of resonances as a function of the neutron energy is shown in Fig. 13a and b for ^{79}Br and ^{81}Br, respectively. This figure provides an efficient method to investigate the population and missing levels. The average s-wave level spacings D_0 are directly related to the inverse slope of these plots and can be obtained from the linear least-squares fits indicated by the straight lines as 57.397 eV and 27.855 eV for ^{79}Br and ^{81}Br, respectively. The points fall below the fitted straight line, indicating that the levels were missed in the resonance analysis. In addition, the average radiative widths $\langle\Gamma_\gamma\rangle$ were calculated using the SAMMY fitted resonance parameters, which were 287.3±10.3 meV and 295.5±12.5 meV for ^{79}Br and ^{81}Br, respectively.

4.3 MACSs

In the continuum region below 370 keV, average cross sections were obtained with a resolution of 20 bins per decade. The averaged cross section relative to the gold sample $\sigma_{\text{Br}}(E_{\text{n}})$ is given by

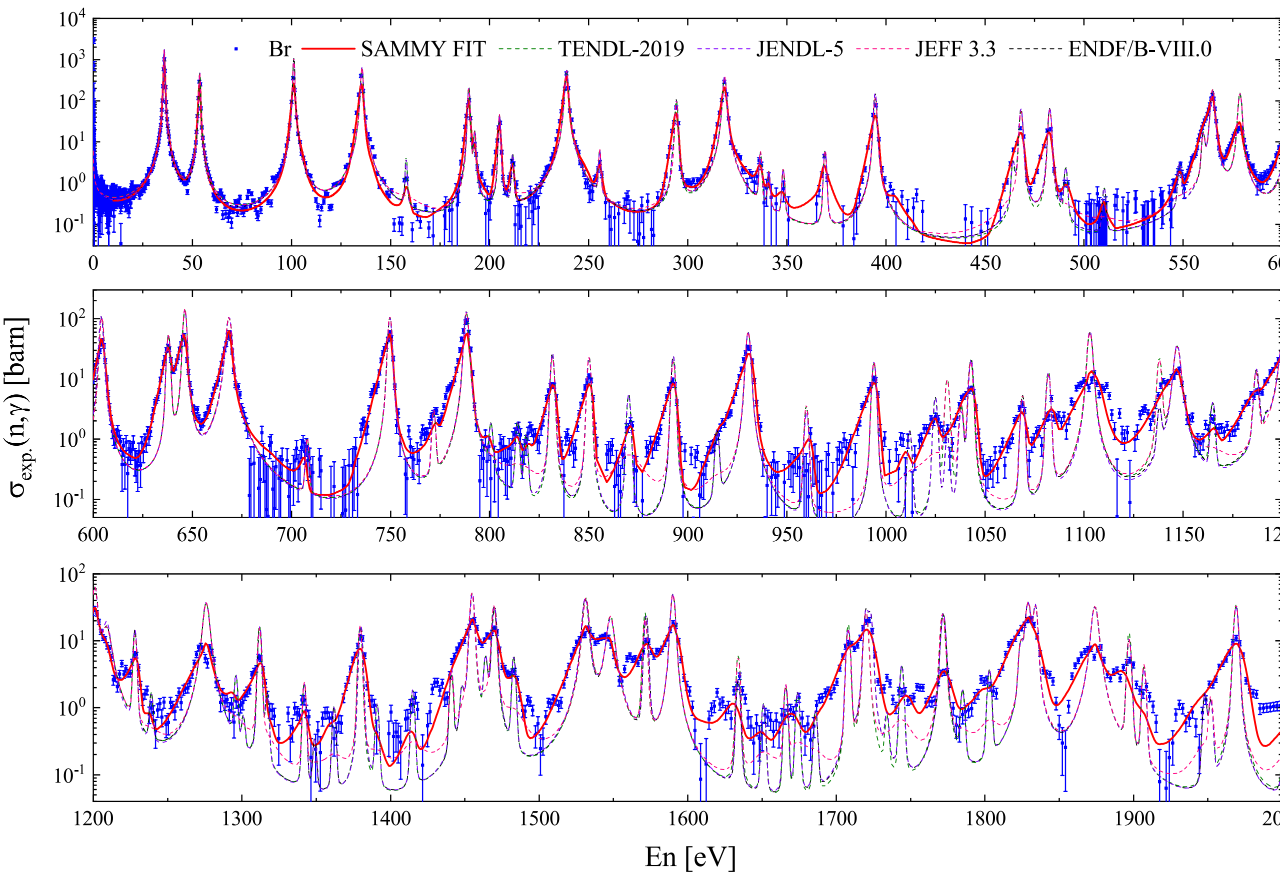

Fig. 12 (Color online) Capture cross section $\sigma_{\text{exp.}}(\text{n},\gamma)$ calculated from the experimental yields obtained in this study (black dots). The SAMMY fitted yield (red solid line) and evaluated databases are plotted for comparison

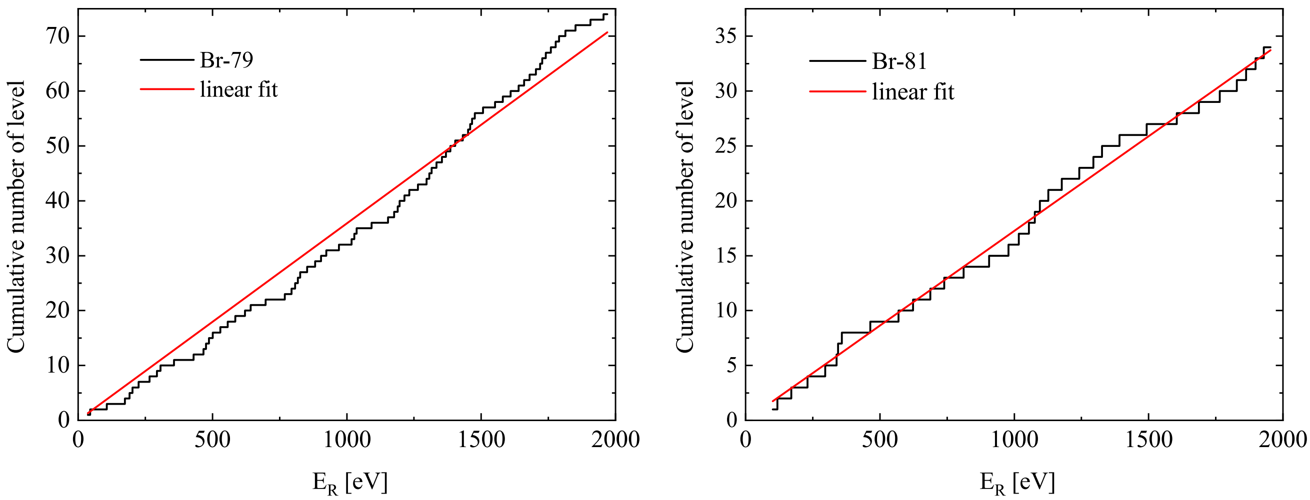

Fig. 13 (Color online) Staircase plots of the cumulative numbers of resonances in the investigated bromine isotopes

$$\sigma_{\mathrm{Br}}(E_{\mathrm{n}}) = \frac{\sigma_{\mathrm{Au}}(E_{\mathrm{n}})}{\langle\sigma_{\mathrm{Au}}(E_{\mathrm{n}})\rangle}\langle\sigma_{\mathrm{Br}}(E_{\mathrm{n}})\rangle, \tag{14}$$

where $\langle\sigma_{\mathrm{Au}}(E_{\mathrm{n}})\rangle$ and $\langle\sigma_{\mathrm{Br}}(E_{\mathrm{n}})\rangle$ are the experimental values measured in this study and $\sigma_{\mathrm{Au}}(E_{\mathrm{n}})$ is the evaluated value obtained from the ENDF/B-VIII.0 database. The uncertainty of the standard ^{197}Au cross section recommended by the ENDF/B-VIII.0 library was estimated to be of the order of 6.0% below 200 keV and 4.0% between 200 and 300 keV. In the URR, the average cross section of K was lower than that of Br by two orders of magnitude, and the neutron capture events of K atoms could be ignored in this region. Finally, the results of the cross section of Br in the continuum region from 10 to 370 keV are given in 20 bins per decade in Table 3.

Table 3 Average capture cross sections of natural bromine in the URR. σ_{Br} calculated with the Li–Si neutron spectrum is also given in this table

E_{low} (keV)	E_{up} (keV)	σ_{Br} (^{197}Au) (mb)	σ_{Br} (Li–Si) (mb)	E_{low} (keV)	E_{up} (keV)	σ_{Br} (^{197}Au) (mb)	σ_{Br} (Li–Si) (mb)
2.0	2.3	2554.0 ± 247.6	2554.0 ± 247.6	27.2	30.8	658.5 ± 61.1	728.3 ± 77.3
2.3	2.6	3063.6 ± 291.7	3063.6 ± 291.7	30.8	34.9	527.1 ± 48.7	477.0 ± 51.5
2.6	2.9	2642.6 ± 250.4	2642.6 ± 250.4	34.9	39.5	560.1 ± 51.7	588.4 ± 61.2
2.9	3.3	2475.0 ± 234.6	2475.0 ± 234.6	39.5	44.7	496.1 ± 45.6	490.3 ± 53.3
3.3	3.7	1834.4 ± 173.7	1834.4 ± 173.7	44.7	50.6	430.3 ± 39.5	398.6 ± 41.5
3.7	4.2	2146.6 ± 203.4	2146.6 ± 203.4	50.6	57.3	438.8 ± 40.2	435.6 ± 47.5
4.2	4.8	2261.1 ± 214.2	2261.1 ± 214.2	57.3	64.9	368.7 ± 33.6	332.6 ± 36.9
4.8	5.4	1251.1 ± 118.6	1081.1 ± 118.6	64.9	73.5	337.6 ± 30.7	316.0 ± 34.4
5.4	6.1	1314.9 ± 124.4	1511.4 ± 160.1	73.5	83.3	310.7 ± 28.2	283.7 ± 30.2
6.1	6.9	1445.7 ± 136.6	1389.3 ± 139.6	83.3	94.3	335.6 ± 30.3	348.1 ± 38.2
6.9	7.8	1516.2 ± 143.2	1543.1 ± 157.9	94.3	106.8	302.9 ± 27.3	308.5 ± 31.3
7.8	8.9	1249.5 ± 117.9	1282.5 ± 131.5	106.8	120.9	273.8 ± 24.6	270.5 ± 29.7
8.9	10.1	1300.4 ± 122.5	1416.5 ± 148.9	120.9	136.9	236.4 ± 21.1	213.4 ± 24.1
10.1	11.4	1141.4 ± 122.5	1175.2 ± 121.3	136.9	155.0	251.8 ± 22.4	251.8 ± 28.3
11.4	12.9	1211.3 ± 107.3	1223.5 ± 127.5	155.0	175.5	243.0 ± 21.5	251.9 ± 27.9
12.9	14.6	874.8 ± 78.8	824.1 ± 88.9	175.5	198.7	209.3 ± 18.4	191.5 ± 20.9
14.6	16.5	875.2 ± 82.1	882.8 ± 92.4	198.7	225.0	204.1 ± 17.9	202.9 ± 21.1
16.5	18.7	840.1 ± 78.5	847.1 ± 89.1	225.0	254.8	186.0 ± 16.2	200.7 ± 21.0
18.7	21.2	845.5 ± 78.8	863.8 ± 91.1	254.8	288.5	152.5 ± 13.2	147.9 ± 15.1
21.2	24.0	738.6 ± 68.8	714.2 ± 74.5	288.5	326.7	131.7 ± 11.4	154.9 ± 15.3
24.0	27.2	575.2 ± 68.8	475.5 ± 52.7	326.7	370.0	112.8 ± 9.7	133.5 ± 14.2

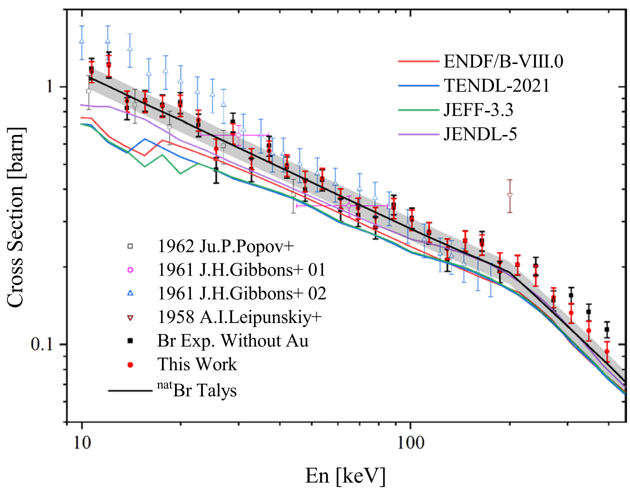

Fig. 14 (Color online) Capture cross sections of bromine in this study relative to the ^{197}Au sample (red square dots). The cross sections calculated using the neutron flux determined by the Li–Si detector are also plotted for comparison

Table 4 MACSs of ^{79}Br and ^{81}Rb

kT (keV)	^{79}Br (mb)		^{81}Br (mb)	
	This study(mb)	KADoNiS v1.0	This study	KADoNiS v1.0
5	1938 ± 194	1890 ± 181	725 ± 73	715 ± 35
10	1272 ± 127	1223 ± 105	534 ± 53	447 ± 27
15	1003 ± 100	966 ± 74	433 ± 43	357 ± 21
20	852 ± 85	823 ± 58	369 ± 37	307 ± 16
25	753 ± 75	729 ± 49	325 ± 33	272 ± 13
30	682 ± 68	661 ± 44	293 ± 29	248 ± 10
40	585 ± 59	567 ± 38	248 ± 25	212 ± 10
50	519 ± 52	503 ± 35	218 ± 22	188 ± 10
60	470 ± 47	454 ± 33	196 ± 20	170 ± 10
80	396 ± 40	383 ± 30	165 ± 17	145 ± 9
100	341 ± 34	332 ± 27	143 ± 14	127 ± 8

As shown in Fig. 14, the average cross sections obtained in this study in the continuum region (red dots) were compared with previous experimental results and the evaluated database. Our measurements are consistent with the results of Gibbons et al. (1961) and the results of Popov et al. (1961), but higher than those of all evaluated databases. For comparison, in this figure, we also plot black dots, which were calculated using the neutron flux determined by the Li–Si detector. In the region over 200 keV, the Li–Si detector-determined results were obviously higher than the results measured with the gold sample. In addition, fluctuations near 30 keV in the results determined by the Li–Si detector were caused by aluminum material in the neutron beam pipe.

The TALYS code was used to describe the isotopic average cross sections in the URR. The calculations were based on the Hauser–Feshbach statistical emission model, which assumes that the capture reactions occur by means of a compound nuclear system that reaches statistical equilibrium. The previously obtained statistical average level space D_0 average radiation width $\langle\Gamma_\gamma\rangle$ was used as the input parameter for the TALYS code calculations. In addition, the global neutron optical model potential in Ref. [41, 42] was used in the calculations. Other parameters were chosen using the method reported in Chen et al. [43], the photon strength function was given by Kopecky and Uhl [45, 46], and the

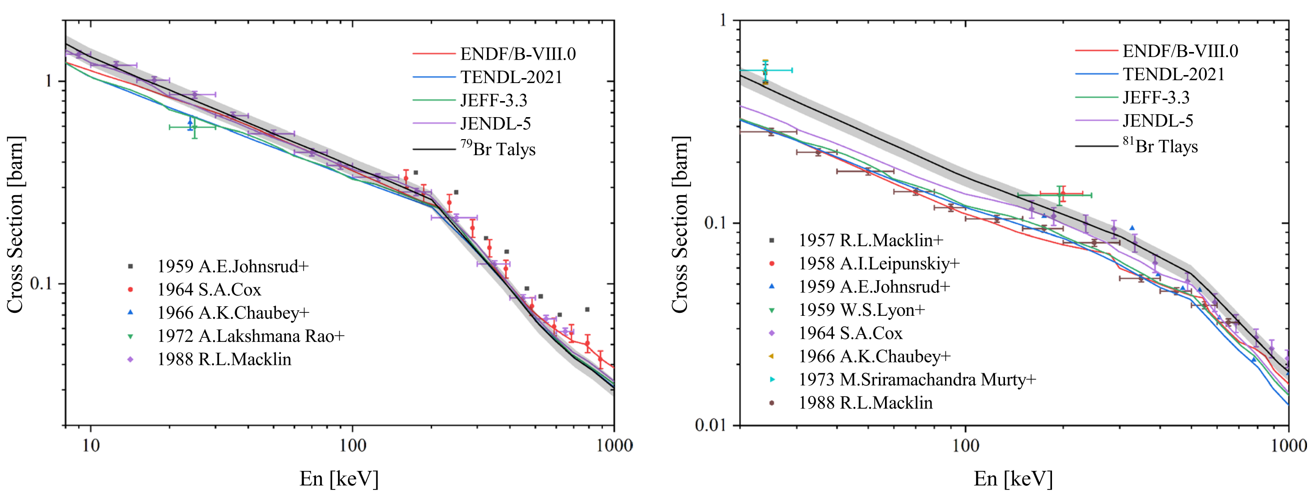

Fig. 15 (Color online) Average capture cross sections of ^{79}Br and ^{81}Br calculated using the TALYS code. The theoretical average cross sections of ^{79}Br are essentially consistent with the previous measurements and evaluated values, whereas those of ^{81}Br roughly agree with the previous measurements but are higher than those of the evaluated database

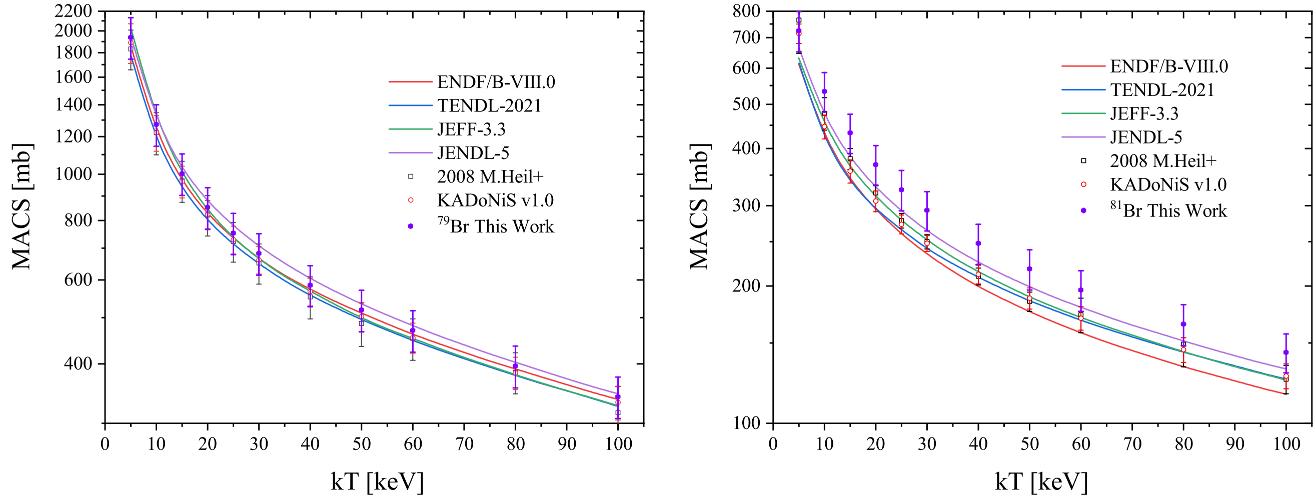

Fig. 16 (Color online) MACSs calculated using Eq. (15) for ^{79}Br and ^{81}Br, respectively

level density a and nuclear temperature T were given by the Gilbert-Cameron model with adjusted parameters. In addition, $\langle\Gamma_\gamma\rangle$ was systematically multiplied by a factor of 0.9 for both isotopes to obtain the γ transmission coefficient. The calculated capture cross sections effectively reproduced the available experimental average cross sections of ^{79}Br and ^{81}Br, as illustrated in Fig. 15.

From these average cross-section values in Fig. 15, the Maxwell average cross sections (MACSs) of ^{79}Br and ^{81}Br were calculated for thermal energies kT ranging from 5 to 100 keV according to

$$\langle\sigma\rangle_{kT} = \frac{2}{\sqrt{\pi}} \frac{\int_0^\infty \sigma(E_\mathrm{n}) E_\mathrm{n} \mathrm{e}^{-E_\mathrm{n}/kT} \mathrm{d}E_\mathrm{n}}{\int_0^\infty E_\mathrm{n} \mathrm{e}^{-E_\mathrm{n}/kT} \mathrm{d}E_\mathrm{n}}, \tag{15}$$

and the corresponding results are listed in Table 4, respectively.

Figure 16 shows a comparison of our results, the evaluated databases, and the recommended values compiled in the Karlsruhe Astrophysical Database of Nucleosynthesis in Stars (KADoNiS)[47]: (a) the MACS values of ^{79}Br obtained in this study, which were essentially located between the values of the JEFF-3.3 [48], TENDL-2021[49], ENDF/B-VIII.0[50], and JENDL-5[51] databases, are in good agreement with the KADoNiS v1.0 values; (b) for ^{81}Br, the calculated values were considerably

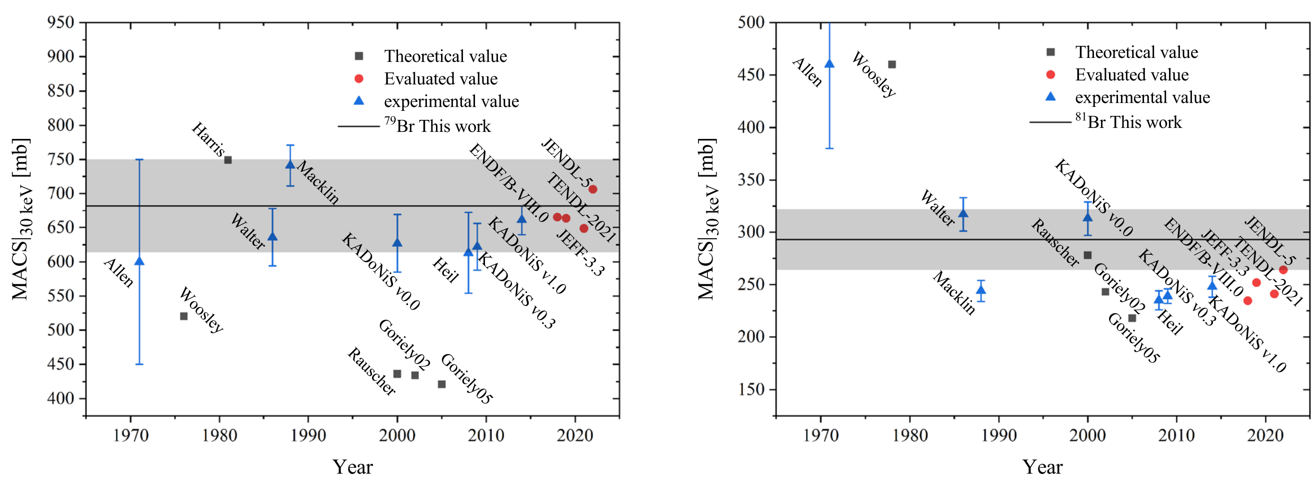

Fig. 17 MACSs at a thermal energy of $kT = 30$ keV for ^{79}Br and ^{81}Br. The blue triangles represent previous experimental results: Heil et al. [3, 5], Macklin [12], Walter et al. [44], and Allen et al. [52], whereas the three dots labeled KADoNiS v0.0, KADoNiS v0.3, and KADoNiS v1.0 are the recommended values from three version of the KADoNiS database. The red dots labeled ENDF/B-VIII.0, JEFF-3.3, TENDL-2021, and JENDL-5 are calculated from the evaluated databases according to Eq. (15). The black dots represent the theoretical values taken from Goriely [54], Rauscher et al. [55], Harris [53], and Woosley et al. [4]

Table 5 Resonance parameters extracted via SAMMY [38] fit to our experimental data. The resonance parameters from ENDF/B-VIII.0 [50] are listed for comparison

Nuclei	*J*	This study		ENDF/B-VIII.0[50]		Nuclei	*J*	This work		ENDF/B-VIII.0[50]	
		E_{exp}[eV]	k_{exp}[meV]	E_{endf}[eV]	k_{endf}[meV]			E_{exp}[eV]	k_{exp}[meV]	E_{endf}[eV]	k_{endf}[meV]
^{79}Br	2	35.82 ± 0.02	12.08 ± 0.52	35.8	22.5	^{81}Br	2	1106.03 ± 0.25	98.75 ± 3.49	1103.0	103.44
^{79}Br	1	53.74 ± 0.02	10.67 ± 0.62	53.7	10.9	^{79}Br	2	1140.99 ± 0.44	3.58 ± 0.68	1138.0	3.4
^{81}Br	2	101.25 ± 0.04	44.08 ± 1.66	101.2	56.83	^{81}Br	1	1147.39 ± 0.24	93.47 ± 4.6	1147.0	89.5
^{81}Br	1	135.64 ± 0.05	50.08 ± 6.31	135.6	65.5	^{79}Br	1	1165.64 ± 0.03	4.83 ± 0.85	1165.0	4.8
^{79}Br	2	158.93 ± 0.06	0.24 ± 0.05	157.9	0.3	^{79}Br	1	1186.49 ± 0.28	15.89 ± 2.79	1187.0	20.5
^{79}Br	1	189.59 ± 0.04	21.4 ± 0.94	189.5	23.9	^{79}Br	1	1192.33 ± 1.15	1.17 ± 0.23	1192.0	1.2
^{79}Br	2	192.64 ± 0.07	1.11 ± 0.11	192.5	1.9	^{79}Br	2	1201.44 ± 0.33	164.81 ± 12.11	1201.0	177.9
^{81}Br	1	205.17 ± 0.04	5.94 ± 0.26	205.0	5.41	^{81}Br	1	1207.23 ± 0.81	88.0 ± 13.31	1209.0	84.55
^{79}Br	2	211.78 ± 0.07	0.6 ± 0.04	211.6	0.6	^{79}Br	2	1228.64 ± 0.23	29.02 ± 1.9	1228.0	21.2
^{79}Br	2	238.76 ± 0.05	117.32 ± 4.64	238.9	120.9	^{79}Br	2	1236.61 ± 0.14	1.97 ± 0.39	1239.0	2.0
^{81}Br	2	255.95 ± 0.10	0.46 ± 0.04	255.6	0.55	^{81}Br	2	1276.64 ± 0.36	85.82 ± 3.43	1276.0	147.95
^{79}Br	1	292.13 ± 0.47	0.65 ± 0.12	292.5	0.6	^{79}Br	2	1293.52 ± 0.09	4.39 ± 0.86	1296.0	4.4
^{79}Br	1	294.48 ± 0.06	23.68 ± 1.77	294.3	22.1	^{79}Br	2	1300.82 ± 1.24	0.74 ± 0.15	1301.0	0.8
^{79}Br	2	318.84 ± 0.07	124.39 ± 5.36	318.6	122.7	^{79}Br	2	1312.89 ± 0.18	27.21 ± 2.86	1312.0	23.7
^{81}Br	2	336.87 ± 0.21	0.78 ± 0.1	336.7	0.74	^{81}Br	3	1312.17 ± 1.18	2.31 ± 0.44	1312.0	2.25
^{81}Br	1	341.07 ± 0.54	0.13 ± 0.02	340.9	0.13	^{79}Br	2	1317.76 ± 0.29	2.4 ± 0.47	1317.0	2.4
^{81}Br	2	347.92 ± 0.45	0.29 ± 0.06	348.2	0.3	^{81}Br	3	1340.78 ± 0.06	2.68 ± 0.53	1342.0	2.7
^{81}Br	3	369.44 ± 0.11	1.39 ± 0.1	369.3	1.13	^{79}Br	2	1349.20 ± 1.37	0.49 ± 0.1	1349.0	0.5
^{79}Br	2	395.31 ± 0.07	36.84 ± 3.29	394.6	47.4	^{79}Br	2	1358.55 ± 0.09	1.68 ± 0.33	1362.0	1.7
^{79}Br	2	465.24 ± 0.24	1.06 ± 0.21	464.2	1.1	^{79}Br	1	1379.84 ± 0.18	59.27 ± 4.18	1380.0	31.01
^{79}Br	1	468.79 ± 0.10	20.44 ± 1.52	468.2	26.2	^{79}Br	2	1390.90 ± 1.42	2.16 ± 0.38	1391.0	1.9
^{79}Br	1	482.98 ± 0.13	22.0 ± 1.81	482.7	27.7	^{79}Br	2	1416.77 ± 1.10	4.71 ± 0.69	1415.0	3.3
^{79}Br	2	491.55 ± 0.25	0.94 ± 0.13	490.8	0.9	^{81}Br	3	1442.50 ± 0.07	3.88 ± 0.76	1441.0	3.86
^{79}Br	2	510.28 ± 0.53	0.25 ± 0.05	510.2	0.3	^{79}Br	2	1447.66 ± 1.49	2.45 ± 0.48	1448.0	2.4
^{79}Br	1	548.78 ± 0.23	1.56 ± 0.16	548.2	1.3	^{79}Br	2	1454.83 ± 0.27	159.58 ± 8.84	1455.0	128.3
^{81}Br	1	560.05 ± 0.29	6.95 ± 0.99	560.2	6.89	^{79}Br	2	1463.91 ± 1.43	9.92 ± 1.83	1464.0	9.6
^{79}Br	2	564.98 ± 0.07	159.43 ± 9.44	564.9	117.7	^{79}Br	1	1469.54 ± 0.24	126.27 ± 8.53	1470.0	81.7
^{81}Br	2	578.62 ± 0.32	10.98 ± 1.48	578.7	94.1	^{79}Br	2	1483.27 ± 0.34	22.05 ± 1.51	1483.0	10.8
^{79}Br	1	604.79 ± 0.07	74.95 ± 2.2	604.0	78.0	^{79}Br	2	1531.28 ± 0.48	110.77 ± 11.92	1531.0	170.7
^{79}Br	1	638.07 ± 0.08	42.04 ± 3.25	637.9	33.2	^{81}Br	2	1543.09 ± 0.48	164.81 ± 12.06	1548.0	128.81
^{79}Br	2	645.92 ± 0.08	104.0 ± 3.18	646.2	98.83	^{79}Br	2	1572.06 ± 0.33	67.93 ± 5.44	1572.0	53.2
^{81}Br	2	668.57 ± 0.10	94.42 ± 2.75	668.5	133.86	^{79}Br	2	1590.14 ± 0.21	168.89 ± 9.75	1590.0	151.1
^{81}Br	0	707.04 ± 0.15	0.58 ± 0.11	708.0	0.59	^{79}Br	1	1630.24 ± 0.10	6.68 ± 1.19	1634.0	5.81
^{79}Br	2	749.73 ± 0.08	112.09 ± 9.76	749.7	89.2	^{79}Br	2	1648.59 ± 0.11	2.54 ± 0.5	1651.0	2.5
^{81}Br	1	771.87 ± 0.26	0.86 ± 0.12	771.8	0.67	^{81}Br	2	1667.03 ± 0.31	2.69 ± 0.53	1666.0	2.74
^{79}Br	2	789.03 ± 0.10	101.74 ± 16.57	788.3	138.1	^{79}Br	2	1671.64 ± 0.09	3.95 ± 0.77	1674.0	3.9
^{79}Br	1	800.20 ± 0.67	0.69 ± 0.15	800.7	1.2	^{79}Br	1	1688.90 ± 1.58	2.26 ± 0.39	1686.0	2.0
^{79}Br	2	815.01 ± 0.59	1.67 ± 0.25	814.1	1.5	^{81}Br	1	1707.18 ± 0.68	34.73 ± 4.43	1708.0	35.63
^{79}Br	1	819.85 ± 0.68	1.06 ± 0.18	818.4	0.9	^{79}Br	1	1718.49 ± 0.53	112.25 ± 13.78	1720.0	87.1
^{79}Br	2	832.52 ± 0.10	21.36 ± 1.59	831.7	23.2	^{79}Br	1	1720.80 ± 0.58	75.28 ± 9.91	1723.0	65.9
^{81}Br	1	850.90 ± 0.10	20.86 ± 2.01	850.2	20.11	^{79}Br	1	1734.14 ± 0.95	1.6 ± 0.32	1734.0	1.6
^{79}Br	2	871.50 ± 0.09	4.28 ± 0.83	870.2	4.9	^{79}Br	2	1746.83 ± 0.06	10.8 ± 2.01	1744.0	10.4
^{79}Br	2	893.16 ± 0.11	23.97 ± 1.25	892.7	21.8	^{79}Br	1	1772.20 ± 0.33	40.79 ± 2.1	1772.0	86.9
^{79}Br	2	915.83 ± 0.14	1.31 ± 0.26	914.8	1.3	^{79}Br	2	1782.61 ± 1.36	3.66 ± 0.74	1785.0	4.3
^{79}Br	1	931.66 ± 0.11	92.9 ± 7.94	930.5	72.5	^{79}Br	1	1797.38 ± 0.08	8.95 ± 1.68	1803.0	9.2

Table 5 (continued)

Nuclei	J	This study		ENDF/B-VIII.0[50]		Nuclei	J	This work		ENDF/B-VIII.0[50]	
		$E_{exp.}$[eV]	$k_{exp.}$[meV]	E_{endf}[eV]	k_{endf}[meV]			$E_{exp.}$[eV]	$k_{exp.}$[meV]	E_{endf}[eV]	k_{endf}[meV]
^{81}Br	1	961.98 ± 0.08	1.23 ± 0.23	959.9	1.2	^{81}Br	2	1822.50 ± 0.28	10.83 ± 1.92	1824.0	10.84
^{81}Br	1	994.59 ± 0.13	33.02 ± 2.39	994.0	20.65	^{79}Br	2	1829.69 ± 1.00	165.65 ± 25.0	1829.0	172.5
^{79}Br	2	1009.96 ± 0.72	1.78 ± 0.29	1012.0	1.5	^{81}Br	2	1834.21 ± 0.57	86.82 ± 14.21	1834.0	96.19
^{79}Br	1	1025.15 ± 0.30	7.88 ± 0.59	1025.0	5.6	^{79}Br	2	1872.34 ± 0.57	86.24 ± 4.93	1874.0	191.8
^{79}Br	2	1029.89 ± 0.19	1.2 ± 0.24	1031.0	1.2	^{81}Br	1	1891.79 ± 0.06	30.41 ± 4.45	1897.0	29.44
^{81}Br	3	1039.82 ± 0.42	2.81 ± 0.55	1038.0	2.87	^{81}Br	1	1904.58 ± 0.07	3.67 ± 0.65	1907.0	3.66
^{79}Br	2	1043.65 ± 0.16	29.06 ± 1.66	1043.0	25.7	^{79}Br	2	1942.35 ± 0.07	4.62 ± 0.9	1948.0	4.6
^{81}Br	3	1069.00 ± 0.22	7.85 ± 0.41	1069.0	4.51	^{81}Br	3	1953.94 ± 0.43	2.52 ± 0.5	1952.0	2.53
^{81}Br	1	1083.89 ± 0.14	13.07 ± 1.98	1082.0	14.57	^{79}Br	2	1969.17 ± 0.26	161.57 ± 13.28	1969.0	108.2

higher than those of the evaluated database and the KADoNiS v1.0 recommended values.

Figure 17 shows a comparison of our results with the previously recommended MACSs from the experimental results[52], evaluated databases and theoretical values[53–55] in nuclear astrophysics concerned with a thermal energy of kT = 30 keV. The value of 682±68 mb for ^{79}Br shown in Fig. 17a is in good agreement with the KADoNiS v1.0 recommended value of 661±44 mb within the uncertainty range. However, the MACS value of 293±29 mb for ^{81}Br shows a clear discrepancy from the KADoNiS v1.0 recommend value of 248±10 mb.

5 Conclusion

The (n,γ) reaction of natural bromine was measured at the Back-n facility using an array of four C_6D_6 detectors. The PHWT with Monte Carlo simulations and the double-bunch unfolding method were used for data preprocessing. The black resonance method with a Ta–Ag–Co filter and dedicated measurements were used to study the experimental backgrounds and obtain accurate backgrounds.

Capture yields were analyzed in the RRR using the R-matrix code SAMMY. A total of 121 resonances were observed in the neutron energy range of 1 to approximately 2000 eV. From these results, the average level spacing, radiative widths, and neutron strength functions were deduced via statistical analyses to establish a consistent set of input data for detailed cross-section calculations using the Hauser-Feshbach statistical model. The MACSs for ^{79}Br obtained in this study were located between the JEFF-3.3, TENDL-2021, ENDF/B-VIII.0, and JENDL-5 databases and are in good agreement with the KADoNiS v1.0 values. In contrast, for ^{81}Br, the calculated values were substantially higher than those of the evaluated database and the KADoNiS v1.0 recommended values. The MACSs at kT = 30 keV were 682±68 and 293±29 mb for ^{79}Br and ^{81}Br, respectively. Our results provide additional constraints on the actual MACSs of ^{79}Br and ^{81}Br.

Author contributions All authors contributed to the study conception and design. Material preparation, data collection and analysis were performed by Zhen-Dong An, Wei Jiang and Jie Ren. The first draft of the manuscript was written by Zhen-Dong An, and all authors commented on previous versions of the manuscript. All authors read and approved the final manuscript.

Data availability The data that support the findings of this study are openly available in Science Data Bank at https://www.doi.org/10.57760/sciencedb.12614, https://www.doi.org/10.57760/sciencedb.j00186.00297, https://www.doi.org/10.57760/sciencedb.j00186.00298, https://www.doi.org/10.57760/sciencedb.j00186.00299 and https://cstr.cn/31253.11.sciencedb.12614, https://cstr.cn/31253.11.sciencedb.j00186.00297, https://cstr.cn/31253.11.sciencedb.j00186.00298, https://cstr.cn/31253.11.sciencedb.j00186.00299.

Declarations

Conflict of interest Chun-Wang Ma and Jing-Yu Tang are editorial board members for Nuclear Science and Techniques and were not involved in the editorial review, or the decision to publish this article. All authors declare that there are no competing interests.

References

1. C.M. Raiteri, M. Busso, G. Picchio et al., S-process nucleosynthesis in massive stars and the weak component. I–evolution and neutron captures in a 25 solar mass star. Astrophys. J. **371**, 11 (1991). https://doi.org/10.1086/169932
2. P.A. Egelstaff, B.T. Taylor, Slow neutron cross-sections of molybdenum and bromine. Nature **166**, 825 (1950). https://doi.org/10.1038/166825b0
3. M. Heil, M. Pignatari, The weak s-process and its relation to explosive nucleosynthesis. In AIP Conferences Proceedings. vol. 819, p. 265 (2006). https://doi.org/10.1063/1.2187869
4. S.E. Woosley, W.A. Fowler, J.A. Holmes et al., Semiempirical thermonuclear reaction-rate data for intermediate-mass nuclei. At.

Data Nucl. Data Tables **22**, 371 (1978). https://doi.org/10.1016/0092-640x(78)90018-9
5. M. Heil, F. Käppeler, E. Uberseder et al., Stellar (n,γ) cross sections for Br and Rb: matching the weak and mains-process components. Phys. Rev. C **78**, 025802 (2008). https://doi.org/10.1103/PhysRevC.78.025802
6. K.S. Krane, Cross sections and isomer ratios in the Rb(n,γ) and Sr(n,γ) reactions. Eur. Phys. J. A **57**, 19 (2021). https://doi.org/10.1140/epja/s10050-020-00299-2
7. C.O. Muehlhause, Neutron capture gamma-ray multiplicity. Phys. Rev. **79**, 277 (1950). https://doi.org/10.1103/PhysRev.79.277
8. J.H. Muehlhause, R.L. Macklin, P.D. Miller et al., Average radiative capture cross sections for 7-to 170-keV neutrons. Phys. Rev. **122**, 182 (1961). https://doi.org/10.1103/PhysRev.122.182
9. J.W. Meadows, J.F. Whalen, Thermal neutron absorption cross sections by the pulsed source method. Nucl. Sci. Eng. **9**, 132 (2017). https://doi.org/10.13182/nse61-a15597
10. J.H. Gibbons, R.L. Macklin, P.D. Miller et al., Average radiative capture cross sections for 7-to 170-keV neutrons. Phys. Rev. **122**, 182 (1961). https://doi.org/10.1103/PhysRev.122.182
11. M. Ohkubo, Y. Kawarasaki, M. Mizumoto, Neutron resonance parameters of bromine-79 and bromine-81. J. Nucl. Sci. Tech. **18**(10), 745–755 (1981). https://doi.org/10.1080/18811248.1981.9733316
12. R.L. Macklin, Neutron capture by ^{79}Br, ^{81}Br, and ^{75}As. Nucl. Sci. Eng. **99**(2), 133–144 (1988). https://doi.org/10.13182/NSE88-A23554
13. Q. An, H.Y. Bai, J. Bao et al., Back-n white neutron facility for nuclear data measurements at CSNS. J. Instrum. **12**, P07022 (2017). https://doi.org/10.1088/1748-0221/12/07/p07022
14. X.X. Li, L.X. Liu, W. Jiang et al., New experimental measurement of ^{nat}Er(n,γ) cross sections between 1 and 100 eV. Phys. Rev. C **104**, 054302 (2021). https://doi.org/10.1103/PhysRevC.104.054302
15. X.X. Li, L.X. Liu, W. Jiang et al., Experimental determination of the neutron resonance peak of ^{162}Er at 67.8 eV. Phys. Rev. C **106**, 065804 (2022). https://doi.org/10.1103/PhysRevC.106.065804
16. S. Zhang, G. Li, W. Jiang et al., Measurement of the ^{159}Tb(n,γ) cross section at the CSNS Back-n facility. Phys. Rev. C **107**, 045809 (2023). https://doi.org/10.1103/PhysRevC.107.045809
17. X.K. Li, Z.D. An, W. Jiang et al., Measurement of the ^{nat}Eu(n,γ) cross section up to 500 keV at the CSNS Back-n facility, and the stellar ^{151,153}Er(n,γ) cross section at s-process temperatures. Eur. Phys. J. A **58**, 251 (2022). https://doi.org/10.1140/epja/s10050-022-00887-4
18. Z.D. An, W.W. Qiu, W. Jiang et al., Measurement of the ^{181}Ta(n,γ) cross sections up to stellar s-process temperatures at the CSNS Back-n. Sci. Rep. **13**, 12657 (2023). https://doi.org/10.1038/s41598-023-39603-7
19. Q. Li, G. Luan, J. Bao et al., The ^{6}LiF-silicon detector array developed for real-time neutron monitoring at white neutron beam at CSNS. Nucl. Instrum. Methods Phys. Res. Sect. A **946**, 162497 (2019). https://doi.org/10.1016/j.nima.2019.162497
20. J. Ren, X. Ruan, J. Bao et al., The C_6D_6 detector system on the Back-n beam line of CSNS. Radiat. Detect. Technol. Methods **3**, 52 (2019). https://doi.org/10.1007/s41605-019-0129-8
21. H. Chen, X.L. Wang, China's first pulsed neutron source. Nat. Mater. **15**, 689 (2016). https://doi.org/10.1038/nmat4655
22. X.K. Li, Z.D. An, W. Jiang et al., Measurement of the ^{141}Pr(n,γ) cross section up to stellar s-process temperatures at the China Spallation Neutron Source Back-n facility. Phys. Rev. C **108**, 035802 (2023). https://doi.org/10.1103/PhysRevC.108.035802
23. Z.Z. Ren, Y.W. Yang, Y.H. Chen et al., Measurement of the ^{232}Th(n, f) cross section in the 1–200 MeV range at the CSNS Back-n. Nucl. Sci. Tech. **34**, 115 (2023). https://doi.org/10.1007/s41365-023-01271-7
24. X.R. Hu, G.T. Fan, W. Jiang et al., Measurements of the ^{197}Au(n, γ) cross section up to 100 keV at the CSNS Back-n facility. Nucl. Sci. Tech. **32**, 101 (2021). https://doi.org/10.1007/s41365-021-00931-w
25. J. Tang, Q. An, J. Bai et al., Back-n white neutron source at CSNS and its applications. Nucl. Sci. Tech. **32**, 11 (2021). https://doi.org/10.1007/s41365-021-00846-6
26. B. Jiang, J.L. Han, J. Ren et al., Measurement of ^{232}Th (n, γ) cross section at the CSNS Back-n facility in the unresolved resonance region from 4 keV to 100 keV. Chinese Phys. B **31**, 060101 (2022). https://doi.org/10.1088/1674-1056/ac5394
27. X.R. Hu, L.X. Liu, W. Jiang et al., New experimental measurement of ^{nat}Se(n,γ) cross section between 1 eV to 1 keV at the CSNS Back-n facility. Chinese Phys. B **31**, 080101 (2022). https://doi.org/10.1088/1674-1056/ac6ee2
28. X.X. Li, L.X. Liu, W. Jiang et al., Measurements of the ^{107}Ag neutron capture cross sections with pulse height weighting technique at the CSNS Back-n facility. Chinese Phys. B **31**, 038204 (2022). https://doi.org/10.1088/1674-1056/ac48fd
29. D.X. Wang, S.Y.L.T. Zhang, W. Jiang et al., Neutron capture cross section measurements for ^{nat}Lu with different thickness. Acta Phys. Sin. **71**, 072901 (2022). https://doi.org/10.7498/aps.71.20212051
30. R.L. Macklin, J.H. Gibbons, Capture-cross-section studies for 30–220-keV neutrons using a new technique. Phys. Rev. **159**, 1007 (1967). https://doi.org/10.1103/PhysRev.159.1007
31. C. Massimi, P. Koehler, S. Bisterzo et al., Resonance neutron-capture cross sections of stable magnesium isotopes and their astrophysical implications. Phys. Rev. C **85**, 044615 (2012). https://doi.org/10.1103/PhysRevC.85.044615
32. J. Allison, K. Amako, J. Apostolakis et al., Recent developments in GEANT4. Nucl. Instrum. Methods Phys. Res. Sect. A **835**, 186 (2016)
33. J.N. Wilson, B. Haas, S. Boyer et al., Measurements of (n,γ) neutron capture cross-sections with liquid scintillator detectors. Nucl. Instrum. Methods Phys. Res. Sect. A **511**, 388 (2003). https://doi.org/10.1016/j.nima.2016.06.125
34. H. Yi, T.F. Wang, Y. Li et al., Double-bunch unfolding methods for the Back-n white neutron source at CSNS. J. Instrum. **15**, P03026 (2020). https://doi.org/10.1088/1748-0221/15/03/p03026
35. G. D'Agostini, A multidimensional unfolding method based on Bayes' theorem. Nucl. Instrum. Methods Phys. Res. Sect. A **362**, 487 (1995). https://doi.org/10.1016/0168-9002(95)00274-x
36. J. Ren, X. Ruan, W. Jiang et al., Background study for (n,γ) cross section measurements with C_6D_6 detectors at CSNS Back-n. Nucl. Instrum. Methods Phys. Res. Sect. A **985**, 164703 (2021). https://doi.org/10.1016/j.nima.2020.164703
37. C. Massimi, C. Domingo-Pardo, G. Vannini et al., ^{197}Au(n,γ) cross section in the resonance region. Phys. Rev. C **81**, 044616 (2010). https://doi.org/10.1103/PhysRevC.81.044616
38. N. Larson, *Updated users' guide for sammy multilevel R-matrix fits to neutron data using bayes' equation, Report ORNL/TM-9179/R6* (Oak Ridge National Laboratory, USA, 2002)
39. Z.D. An, Z.P. Chen, Y.G. Ma et al., Astrophysical S factor of the ^{12}C(α,γ)^{16}O reaction calculated with reduced R-matrix theory. Phys. Rev. C **92**, 045802 (2015). https://doi.org/10.1103/PhysRevC.92.045802
40. B. Jiang, J. Han, W. Jiang et al., Monte–Carlo calculations of the energy resolution function with Geant4 for analyzing the neutron capture cross section of ^{232}Th measured at CSNS Back-n. Nucl. Instrum. Methods Phys. Res. Sect. A **1013**, 165677 (2021). https://doi.org/10.1016/j.nima.2021.165677
41. A.J. Koning, J.P. Delaroche, Local and global nucleon optical models from 1 keV to 200 MeV. Nucl. Phys. A **713**, 231 (2003)

42. B. Allen, J. Gibbons, R. Macklin, Nucleosynthesis and neutron-capture cross sections. Advances in nuclear physics, Springer, Berlin, pp .205–259 (1971)
43. S. Chen, P. Tamagno, D. Bernard et al., From nuclear physics to displacement damage calculation and uncertainty propagation in CONRAD. Results Phys. **17**, 103023 (2020). https://doi.org/10.1016/j.rinp.2020.103023
44. G. Walter, H. Beer, F. Kaeppeler et al., The s-process branching at Se-79. Astron. Astrophys. **167**, 186 (1986)
45. J. Kopecky, M. Uhl, Test of gamma-ray strength functions in nuclear reaction model calculations. Phys. Rev. C **41**, 1941 (1990). https://doi.org/10.1103/PhysRevC.41.1941
46. Z.D. An, Y.G. Ma, G.T. Fan et al., New Astrophysical Reaction Rate for the ^{12}C(α,γ)^{16}O Reaction. Astrophys. J. Lett. **817**, L5 (2016). https://doi.org/10.3847/2041-8205/817/1/L5
47. I. Dillmann, T. Szücs, R. Plag et al., The Karlsruhe astrophysical database of nucleosynthesis in stars project–status and prospects. Nucl. Data Sheets **120**, 171 (2014)
48. A.J.M. Plompen, O. Cabellos, D.S.C. Jean et al., The joint evaluated fission and fusion nuclear data library, JEFF-3.3. Eur. Phys. J. A **56**, 181 (2020). https://doi.org/10.1140/epja/s10050-020-00141-9
49. A.J. Koning, D. Rochman, J.C. Sublet et al., TENDL: complete nuclear data library for innovative nuclear science and technology. Nucl. Data Sheets **155**, 1 (2019). https://doi.org/10.1016/j.nds.2019.01.002
50. D.A. Brown, M.B. Chadwick, R. Capote et al., ENDF/B-VIII.0: the 8th major release of the nuclear reaction data library with CIELO-project cross sections, new standards and thermal scattering data. Nucl. Data Sheets **148**, 1 (2018). https://doi.org/10.1016/j.nds.2018.02.001
51. Z. Ge, O. Iwamoto, N. Iwamoto et al., Status of JENDL. In: EPJ Web of Conferences. vol. 239, p. 09002 (2020). https://doi.org/10.1051/epjconf/202023909002
52. B.J. Allen, J.H. Gibbons, R.L. Macklin, Nucleosynthesis and neutron-capture cross sections. Adv. Nucl. Phys. **4**, 205 (1971)
53. M.J. Harris, 30 keV (n,γ) cross-sections from the nuclear statistical model. Comput. Phys. Commun. **21**, 407 (1981). https://doi.org/10.1016/0010-4655(81)90017-5
54. S. Goriely, Hauser–Feshbach rates for neutron capture reactions (version 8/29/2005), (2005). http://www-astro.ulb.ac.be/Html/hfr.html
55. T. Rauscher, F. Thielemann, Astrophysical reaction rates from statistical model calculations. At. Data Nucl. Data Tables **75**, 1 (2000). https://doi.org/10.1006/adnd.2000.0834

Authors and Affiliations

Gao-Le Yang[1] · Zhen-Dong An[1,2,3,4] · Wei Jiang[5,6] · Xian-Kai Li[1,7] · Wei-Wei Qiu[3,4,8] · Zheng-Fa Liao[3,4,8] · Zi-Yue Zhuang[3,4,8] · Xiao-Ping Zhang[3,4] · Sheng-Li Chen[8] · Chen-Chen Guo[8] · Er-Xi Xiao[8] · Xiao Fang[8] · Xin-Xiang Li[2,7,9] · Xin-Rong Hu[2,9] · Bing Jiang[2,9] · Jin-Cheng Wang[10] · Jie Ren[10] · Wen Luo[7] · Zhi-Chao Zhu[7] · Hao-Yang Lan[7] · Zong-Wei Cao[7] · Xu Ma[10,11] · Ying-Du Liu[11] · Pu-Sen Wang[11] · Yi Yang[12] · Ping Su[12] · Xian-Gai Deng[12] · Wan-Bing He[12] · Chun-Wang Ma[13,14] · Yu-Ting Wang[13,14] · Zhi-Tao Dai[15] · Peng-Qin He[1] · Ren-Guang Tang[1] · Tao Zhou[1] · Jing Wang[1] · Han Yi[5,6] · Yue Zhang[5,6] · Yong-Hao Chen[5,6] · Rui-Rui Fan[5,6] · Ke-Qing Gao[5,6] · Qiang Li[5,6] · Kang Sun[5,6] · Zhi-Xin Tan[5,6] · Min-Hao Gu[5,6] · Han-Tao Jing[5,6] · Jing-Yu Tang[5,6,16] · The CSNS Back-n Collaboration

✉ Zhen-Dong An
anzhendong@mail.sysu.edu.cn

1 School of Physics and Astronomy, Sun Yat-sen University, Zhuhai 519082, China

2 Shanghai Institute of Applied Physics, Chinese Academy of Sciences, Shanghai 201800, China

3 State Key Laboratory of Lunar and Planetary Sciences, Macau University of Science and Technology, Macau 999078, China

4 CNSA Macau Center for Space Exploration and Science, Macau 999078, China

5 Institute of High Energy Physics, Chinese Academy of Sciences, Beijing 100049, China

6 Spallation Neutron Source Science Center, Dongguan 523803, China

7 School of Nuclear Science and Technology, University of South China, Hengyang 421001, China

8 Sino-French Institute of Nuclear Engineering and Technology, Sun Yat-sen University, Zhuhai 519082, China

9 University of Chinese Academy of Sciences, Beijing 100049, China

10 Key Laboratory of Nuclear Data, China Institute of Atomic Energy, Beijing 102413, China

11 School of Materials Science and Engineering, Xiangtan University, Xiangtan 411100, China

12 Key Laboratory of Nuclear Physics and Ion-beam Application (MOE), Institute of Modern Physics, Department of Nuclear Science and Technology, Fudan University, Shanghai 200433, China

13 Institute of Particle and Nuclear Physics, Henan Normal University, Xinxiang 453007, China

14 School of Physics, Henan Normal University, Xinxiang 453007, China

15 Shenzhen Center, Cancer hospital, Chinese Academy of Medical Sciences, Shenzhen 518100, China

16 School of Nuclear Science and Technology, University of Science and Technology of China, Hefei 230027, China